Published in final edited form as:
Nat Nanotechnol. 2009 October ; 4(10): 688–694. doi:10.1038/nnano.2009.231.

Golden carbon nanotubes as multimodal photoacoustic and photothermal high-contrast molecular agents

Jin-Woo Kim[1,*], **Ekaterina I. Galanzha**[2,3], **Evgeny V. Shashkov**[2,4], **Hyung-Mo Moon**[1], and **Vladimir P. Zharov**[2,*]

[1]Department of Biological and Agricultural Engineering and Institute for Nanoscale Materials Science and Engineering, University of Arkansas, Fayetteville, Arkansas 72701, USA

[2]Phillips Classic Laser and Nanomedicine Laboratories, Winthrop P. Rockefeller Cancer Institute, University of Arkansas for Medical Sciences, Little Rock, Arkansas 72205, USA

[3]Saratov State University, Institute of Optics and Biophotonics, Saratov 410012, Russia

[4]Prokhorov General Physics Institute, Moscow 119991, Russia

Abstract

Carbon nanotubes have shown promise as contrast agents for photoacoustic and photothermal imaging of tumours and infections because they offer high resolution and allow deep tissue imaging. However, in vivo applications have been limited by the relatively low absorption displayed by nanotubes at near-infrared wavelengths and concerns over toxicity. Here, we show that gold-plated carbon nanotubes—termed golden carbon nanotubes—can be used as photoacoustic and photothermal contrast agents with enhanced near-infrared contrast (~10^2-fold) for targeting lymphatic vessels in mice using extremely low laser fluence levels of a few mJ cm^{-2}. Antibody-conjugated golden carbon nanotubes were used to map the lymphatic endothelial receptor, and preliminary in vitro viability tests show golden carbon nanotubes have minimal toxicity. This new nanomaterial could be an effective alternative to existing nanoparticles and fluorescent labels for non-invasive targeted imaging of molecular structures in vivo.

Among the various light-absorbing nanoparticles (gold nanoshells, gold nanorods, gold nanocages and others[1–16]), carbon nanotubes in particular have been shown to be promising photothermal (PT) and photoacoustic (PA) contrast agents[17–21]. Carbon nanotubes are well suited for imaging and treating tumours, because they can efficiently transform absorbed energy into PT and are accompanied by other phenomena such as PA waves, microbubbles and so on. Moreover, because they absorb in the near-infrared region (NIR), carbon nanotubes can image more deeply within tissues than other optical modalities. Other attractive features include their high mechanical flexibility, high surface area and small diameter, and their ability to cluster helps enhance PA/PT responses[19].

The clinical relevance of carbon nanotubes, however, has been under debate because of concerns over their toxicity, although there are differences in opinions among investigators[22,23]. Compared with gold nanoparticles, carbon nanotubes have a relatively

*Correspondence and requests for materials should be addressed to J.-W.K. and V.P.Z. jwkim@uark.edu; zharovvladimirp@uams.edu.

Author contributions

J.-W.K. and V.P.Z. conceived and designed the experiments. All authors performed the experiments and discussed the results. J.-W.K., E.I.G and V.P.Z. co-wrote the paper.

Additional information

Supplementary information accompanies this paper at www.nature.com/naturenanotechnology.

low NIR absorption coefficient (1.4×10^9 $M^{-1}cm^{-1}$ for gold nanorods versus 6.2×10^6 $M^{-1}cm^{-1}$ for nanotubes)[10,21], so higher concentrations (that is, 125 pM versus 50 nM, respectively) are required for effective PA/PT diagnosis and therapy.

To overcome these limitations, we created golden carbon nanotubes (GNTs) by depositing a thin layer of gold around the carbon nanotubes. The gold layer acts as an NIR absorption enhancer and could potentially address the issues of toxicity. Here, we report the unique physicochemical features of GNTs and their potential use in nanoparticle-assisted PA/PT technologies. GNTs conjugated with an antibody specific to the lymphatic endothelial hyaluronan receptor-1 (LYVE-1) were used for PA/PT mapping of lymphatic endothelial cells (LECs), which line the internal surface of lymphatic vessels. LECs are in direct contact with cells in the lymph flow (such as immune-related cells, tumour cells and bacteria) and their expression and functional activity are closely correlated with the regulation of important processes like tumour metastasis, cell migration and inflammation[24–28].

The LYVE-1 receptor is one of the most widely used lymphatic endothelial markers and fluorescent labelling has been used to identify them[29,30]. However, the in vivo application of fluorescent labelling is limited by tag-associated problems including cytotoxicity, immune responses, photobleaching, blinking or strong light scattering and background auto-fluorescence[31–34]. In this study, we show that when integrated with an advanced PA and PT technique, GNTs can offer a promising alternative for non-invasive targeted in vivo mapping of the lymphatic system. We also discuss the potential of GNTs for PA molecular detection and PT eradication of metastasis in lymph nodes.

Golden nanotubes as PA and PT contrast agents

The GNTs consisted of a shortened single-walled carbon nanotube core with a diameter of 1.5–2 nm, coated by a thin gold layer 4–8 nm thick (Fig. 1). The GNTs were highly water-soluble, well dispersed, relatively uniform in size and rod-shaped with average dimensions of 100 nm (+36.7 nm) in length and 11 nm (+4.1 nm) in diameter (Fig. 1e–h). They had two or three slight gold bumps with minimal gaps between them (Fig. 1f–h), indicating not only multiple nucleations and their growth on the carbon nanotube but also complete coverage of gold on the carbon nanotube surface. Optical spectral analysis of the GNTs (red line in Fig. 2a) showed a transverse plasmon absorption in the visible region of 520–530 nm (similar to gold nanospheres[7,14]) and a longitudinal resonance peak in the NIR region near 850 nm (similar to gold nanorods[4,7,10]; see Supplementary Fig. S1). Conventional absorption spectra of GNTs in suspension were in good agreement with their PA spectra (blue symbols in Fig. 2a) estimated with an integrated PA/PT microscopy spectrometer (see Supplementary Fig. S2). The plasmon responses of GNTs in the NIR were significantly higher (85–150-fold) at the same concentration than those for the shortened single-walled carbon nanotubes (black line in Fig. 2a). PA signals from the rare GNT clusters with an average size of 250–300 nm were 10–15 times stronger in amplitude than those from the individual GNTs, similar to results for CNT clusters[19].

PT imaging demonstrated high contrasts of individual GNTs, even at low laser fluences in the range 1–10 mJ cm^{-2} at 850 nm (Fig. 2b). The PT image contrast increased with increasing pulse energy (Fig. 2c), accompanied by bubble formation around overheated GNTs, and with the appearance of several overlapping microbubbles from closely located GNTs (Fig. 2d). PT thermolens (Fig. 2e–g) and PA (Fig. 2 h–j) signals demonstrated similar behaviours. In particular, as laser fluences at 850 nm increased, fourphase PA signal behaviour was observed (Fig. 2k): (i) a gradual increase of linear PA signal from 1 to 5 mJ cm^{-2} (inset), (ii) nonlinear PA signal enhancement (~10^2-fold) from 5 to 50 mJ cm^{-2} due to bubble formation around overheated GNTs, (iii) slight saturation of signals between 50 and

200 mJ cm^{-2}, probably due to laserinduced GNT bleaching of thermal origins, and (iv) 'secondary' nonlinear signal enhancement at fluences over 200 mJ cm^{-2}, likely due to thermal explosion of GNTs. Laser pulse number did not affect PA signal amplitudes at low fluences below 30 mJ cm^{-2} (Fig. 2l). However, at high fluences, significant decreases in PA signal amplitudes were observed with an increase in pulse number. This indicates extremely high NIR absorption capacity in GNTs, with very effective conversion of the absorbed energy to thermal energy, leading to damage of the GNTs. The bubble lifetime and size, depending on the laser energy (5–500 mJ cm^{-2}) and GNT clustering, ranged from 20 ns to 6 ms and from 200 nm to 10 mm, respectively. This implies the possibility of well-controlled and highly localized cell damage (with minimal damage to surrounding normal cells) through suitable selection of laser energy.

The efficiency of GNTs as PT sensitizers and PA contrast agents was compared with other nanoparticle-based PA/PT contrast agents, such as gold nanospheres, gold nanorods, gold nanoshells and carbon nanotubes. Comparisons were made on the basis of PA signal amplitudes (Fig. 3a) and bubble-formation thresholds (Fig. 3b), which are useful criteria to estimate the efficiency of laser energy conversion into heat and accompanied phenomena[1,11,19]. Even considering the slight differences in sizes and the potential variations in nanoparticles' spatial dispersity (especially the uncontrollable formation of small nanoclusters), the PA signals of GNTs were higher and correspondingly their bubble-formation thresholds were significantly lower than those of carbon nanotubes and gold nanospheres (50–100-fold) and comparable with those of gold nanorods and nanoshells. The GNT bubble-formation threshold of ~3.8 mJ cm^{-2} is significantly lower than the established NIR laser safety standard levels (20–100 mJ cm^{-2} at wavelengths of 500–1,100 nm)[35], thus rendering the GNTs very promising in translation to humans. The addition of ethanol (40%) to the aqueous GNT solution led to a further decrease of the threshold to 0.9 mJ cm^{-2} owing to more favourable thermodynamic parameters for bubble formation[19,36].

Cell viability and proliferation assays revealed no apparent adverse toxicity effects on live cells after their exposure to various concentrations of GNTs (0.05–0. 5 mg ml^{-1}) for 10 days (see Supplementary Fig. S3). Study of the impact of GNTs on mice vasculature revealed no marked changes in mouse behaviour and lymphatic function (such as the diameters and parameters of phasic contractions, flow velocity, valve activity and cell behaviour in the microvasculature) over 1 month after animal exposure to GNTs according to our established protocol[37]. However, it should be noted that conflicting data have been reported on the toxicity of nanoparticles[38–43], so a full-scale systematic investigation of the toxicity of GNTs is required. Our preliminary toxicity studies are encouraging because GNTs show minimal toxicity at typical doses (that is, ~0.2 mg ml^{-1}) and the concentrations required for NIRPA/PT response are lower than those for other techniques22,23. The use of gold in medicine has been documented for over 50 years, including the clinical testing of colloidal gold nanoparticles to treat rheumatoid arthritis[44]. Recently, gold-based nanoparticles, in particular gold nanoshells (commercial name, AuroLase, Nanospectra Biosciences), and colloidal gold nanospheres conjugated with tumour necrosis factor alpha (Cytimmune Sciences) have been approved for pilot clinical trials for cancer treatments. We therefore believe that gold coating could potentially improve the biocompatibility of carbon nanotubes.

Targeting lymphatic endothelial receptors with GNTs

GNTs conjugated with antibody specific to the LYVE-1 receptor (anti-LYVE-1 antibody) were delivered to the lymphatics and exposed to a laser pulse using an integrated intravital microscope (Fig. 4; see Supplementary Fig. S2). Laser-induced PA/PT effects at relatively low laser energy were used for non-invasive diagnostics, and increased laser energy,

accompanied by microbubble formation, was used for therapy, such as ablating individual cells locally.

The functionalization capability of GNTs was assessed by conjugating with rabbit anti-mouse anti-LYVE-1 antibody through electrostatic interactions between the antibodies and GNTs. Epifluorescence microscopy after attachment of fluorescein-labelled secondary antibodies (see Supplementary Fig. S4a,b) confirmed the capability of GNTs for simple and robust bioconjugation. After antibody conjugation, the GNT absorption peak of the transverse plasmon resonance at 525 nm decreased substantially, and the longitudinal plasmon resonance peak was red shifted to ~1,100 nm without a notable change in its intensity (see Supplementary Fig. S4c). This is related to the changes in the surface characteristics as well as the local refractive index by antibodies on the particles.

PA/PT mapping of nude mouse mesentery within the field of interest (Fig. 5a) was obtained by an automatic scanning microscopic stage with the mouse and a fixed focused laser beam with a diameter of 2–10 mm (larger diameter for deeper tissues due to scattering effects) (Fig. 4b). Both PA and PT techniques demonstrated high absorption sensitivity (four orders of magnitude better than conventional absorption spectroscopy/microscopy) with the capability of visualizing absorption heterogeneities of endogenous low-absorbing thin (10–15 mm) mesenteric structures (Fig. 5d,h). The administration of GNTs conjugated with anti-LYVE-1 antibody to the mesentery of live mice led to the appearance of strong PT and PA signals (Fig. 5e,i), which significantly exceeded those from endogenous backgrounds and were preferentially located in the lymphatic wall. Specifically, the mean signal amplitude from the lymphatic wall was increased from 0.89±0.081 a.u. (background before GNT application) to 64.73±17.548 a.u. (at the 60^{th} minute of GNT action) ($P = 0.0006$) for PA signals and from 0.82±0.079 a.u. to 25.84±6.331 a.u. ($P = 0.0002$) for PT signals. The signal amplitudes were stable during at least 5-h observation in vivo and were similar in shape and amplitude with PA/PT signals obtained from GNT control samples in vitro (see Supplementary Figs S5,S6). There were a few false-positive signals in the interstitium and fluctuating signals in the lymph vessel during the first hour of observation, which might be associated with antibody–GNTs taken up by tissue macrophages and washing-out of unbound antibody–GNTs by lymph flow.

In control studies, PA/PT mapping at the 15th minute after unconjugated GNT administration revealed randomly scattered low-level signals in the tissue interstitium and more profound fluctuating signals in lymphatic flow above the background; however, no signals were observed in the lymphatic wall (Fig. 5f,j). Within the next 60 min, signals became diminished in lymphatics due to their natural washing by the lymph flow; however, a few signals were detected in the interstitium (Fig. 5g,k). The latter signals may be associated with GNTs taken up by tissue macrophages. These findings strongly suggest that the PA/PT signal distributions with antibody–GNT conjugates (Fig. 5e,j) are correlated with the position and local concentration of antibody–GNTs bound to LYVE-1 receptors.

The specificity of anti-LYVE-1 antibodies to the receptors has previously been documented with fluorescent techniques[29,30]. Assessments of different lymph vessels showed highly heterogeneous GNT spatial distributions along lymph vessels and GNTs bound to the surface as clusters rather than as single nanoparticles at multiple discrete points. These heterogeneous patterns are in line with blood vessel wall targeting by quantum dots[45]. However, no sign of large GNT aggregates was observed in the control study with GNTs in vitro in suspension as indicated by the absence of image heterogeneity from high-resolution (~250 nm) optical microscopy or by the lack of enhancement of PA signals from PA scanning with a focused laser beam (10 μm in diameter) across a microscopic slide (data not shown). Thus, in analogy to blood vessels[45,46], the observed phenomena may reflect the

molecular diversity of the intact vessel endothelia in vivo in terms of the differential expression of LYVE-1 receptors on LECs in lymphatics. We also observed strong signals from valve leaflets (indicated by arrows in Fig. 5b).

About a sixfold increase of laser energy (10 to 60 mJ cm^{-2}) led to a nonlinear increase of PA/PT signal amplitudes and an increase of PT signal widths associated with microbubble formation around GNTs. These phenomena were similar to those obtained in vitro (see Supplementary Figs S5,S6). The laser-induced microbubbles led to highly localized (within 5–10 mm) damage of lymphatic walls around the zone of high local concentration of GNTs or their clusters without notable changes in the surrounding tissue (Fig. 5c). In addition, we demonstrated PA detection and PT ablation of individual GNT-labelled tumour cells in lymph nodes in vivo (see Supplementary Figs S7,S8 and Supplementary note 1), encouraging further explorations of GNTs in biomedical applications, in particular non-invasive and target-specific lymphatic diagnosis and therapy.

Conclusions

We have introduced GNTs as new NIR contrast agents for PA/PT imaging/mapping of biotissues and demonstrated their advantages for molecular targeting of specific cell types in vivo. This novel hybrid plasmonic contrast agent, which combines the advantages of gold and carbon nanotubes, presents a unique set of features. The size of GNTs can be changed easily by adjusting the length and diameter of the carbon nanotubes and the thickness of the gold layer. This can be done by controlling the growth time of the gold layer and the carbon nanotube treatment procedure and/or by using different types of carbon nanotubes such as doublewalled and multiwalled carbon nanotubes. The hollow cylindrical core (1–2 nm) and thin gold layer (up to 150–200 atoms only in the gold layer of 2–13 nm) make it an ultralow-weight material. Furthermore, because of its high NIR absorption, only low GNT concentrations are required (pico- to potentially femtomolar) for effective diagnostic and therapeutic applications. This is compared to nanomolar levels for conventional agents47. Although further toxicity investigations are required, our preliminary in vitro toxicity data suggest that GNTs have minimal cytotoxicity. The chemically inert gold coating does not require toxic precursors (such as cetyltrimethylammonium bromide when making gold nanorods) and the low laser fluence suggests it could be clinically applicable[35].

The high surface area on the thin and long GNTs may allow several biomarkers to be conjugated for simultaneous multiplex targeting. With multiplexed tags the percentage of detectable cells within the targeted cell population, such as LECs or tumour cells, can increase from 25–60% (when using mono-antibody tags) to 90–98%. Owing to the synergy of laser-induced optical (plasmon), thermal, acoustic and bubble overlapping phenomena from individual GNTs[3,11], PA and PT effects in GNT clusters are amplified. By changing the length, diameter, aspect ratio and thickness of the gold layer, the GNT absorption can be adjusted for multicolour targeting[20]. The hybrid system also allows a ‘bimodal’ capability for integrated PA/PT diagnosis and therapy. Also the hollow core, which can lower the heat capacity to allow better pulse heating, may also potentially carry therapeutic payloads (such as drugs, magnetic materials, ethanol and other chemicals). Owing to their spatial structure (with a hollow empty core as the ‘long hole’ in GNTs) and high absorption cross-section, which exceeds their geometric cross-section by more than one order of magnitude (see Supplementary note 2), our results also suggest that GNTs could be called ‘black nanoholes’. Photons travelling far outside the GNTs can be ‘trapped’ by them, in analogy to space black holes.

The PT method with pulse laser showed higher sensitivity over the PA method in the mapping of microscale absorbing targets and was capable of not only time-resolved

monitoring of laser-induced thermal and bubble-formation phenomena with high spatial resolution (300 nm) but also rapid (microsecond scales) PT therapy, at least on animal models with relatively transparent tissue structures such as the mesentery or ear[16]. On the other hand, the PA method provided better sensitivity in detecting GNTs, especially in the nonlinear mode, and its backward schematics (that is, laser and transducer on one side) are potentially better suited for assessing deep lymphatic vessels and nodes up to 3–5 cm in humans[14]. These indicate that the PA and PT methods are complementary and, in combination, serve as a powerful tool in nanotechnology-based biomedical research.

We showed that GNTs could target lymphatic vessels in a well established live animal model[37]. Although recent discoveries in the biology of lymphatics have emphasized their key roles in immunity as well as the development of many diseases[24–28,48], compared with molecular targeting of blood vessels[49], lymphatics have been paid much less attention. To date, many questions on lymphatic functions remain unanswered, including in vivo control of lymphangiogenesis and ways to track and eradicate metastatic cells in prenodal lymphatics and the sentinel lymph nodes. GNTs may be used for a variety of biomedical applications including non-invasive and highly target-specific lymphatic diagnosis and therapy. We are currently investigating the potential of GNTs for molecular detection and eradication of metastasis in the sentinel lymph nodes (see Supplementary note 1) and real-time tracking of GNTs in ear and skin animal vasculatures, as well as an in vivo toxicity study of GNTs on animal models.

Methods

GNT synthesis

GNTs were synthesized by interfacing gold and carbon nanotubes, in particular single-walled carbon nanotubes, by means of a gold deposition process without the aid of additional reducing agents such as citrate for colloidal gold preparation or external voltage sources. Single-walled carbon nanotubes play dual roles as substrates as well as reducing agents. Briefly, single-walled carbon nanotubes were purchased from Carbon Nanotechnologies and processed as described previously[50] with an initial concentration of 1 g l^{-1}. The processed nanotubes were reconstituted in water. Estimated with atomic force microscopy (AFM), the resultant nanotubes were well dispersed and shortened, with an average length and diameter of 98.7 nm (±32.72 nm) and 1.7 nm (±0.18 nm), respectively (Fig. 1a–d). The reaction medium for gold deposition consisted of 0.5 ml of the nanotube solution and 9.5 ml of an aqueous solution containing 10 mM $HAuCl_4$. The reaction mixture was incubated at room temperature (23 °C) with gentle mixing. The reaction proceeded over a period of several minutes and was associated with a change in colour from the dark grey characteristic of nanotubes to purple. The resultant GNTs were harvested and washed three times with distilled water after centrifugation at 10,000g for 5 min to remove the remaining reactants, that is, HAuCl4 and nanotubes (see Supplementary note 3).

GNT bioconjugation and toxicity test

GNTs were decorated with rabbit antimouse antibodies to LYVE-1 of LECs (Research Diagnostics) through interactions between antibodies and GNTs according to the manufacturer's specifications for the common antibody conjugation for gold colloids at pH 7.4 (see Supplementary Methods). The GNTs without the primary IgY were used as a negative control. The antibody–GNT conjugates were stained with fluorescein-labelled secondary antibody (ImmunoPurew fluorescein conjugated goat anti-rabbit IgG, Pierce Biotechnology) to validate the antibody conjugation according to the manufacturer's specification using epifluorescence microscopy (see Supplementary Methods). The cytotoxicity of GNTs was assessed by monitoring cell viability and proliferation for 10 days

using CellTiter 96w AQueous one solution cell proliferation assay (Promega) with T98G human glioblastoma cell line (ATCCw # CRL-1690TM, American Type Culture Collection, ATCC) according to the specifications of Promega and ATCC (see Supplementary Methods). The extended incubation time of 10 days was chosen to allow sufficient time for the influence, if any, of GNTs on cell viability. In addition, the effect of GNTs on lymphatic function in vivo on mouse model was estimated by monitoring lymph vessel parameters (diameter, phasic activity, valve function and lymph flow) over 1 month according to our established methodology for the study of nicotine, drug and chemical impacts[37].

GNT assessment

The optical absorption spectra of GNTs were examined using a DU-800 ultraviolet/visible/NIR (UV/vis/NIR) spectrophotometer (Beckman Coulter). The UV/vis/NIR optical spectra were normalized on the maximal absorption of single-walled carbon nanotubes and GNTs at the wavelength range of 300 and 1,100 nm. Similar spectral analyses were also carried out for gold nanorods and gold nanoshells (see Supplementary Fig. S1). The physical characteristics of GNTs after synthesis were assessed using AFMand transmission electron microscopy (TEM) (see Supplementary Methods).

Animal models

The nude mice (nu/nu, weighing 20–25 g), purchased from Harlan Sprague–Dawley, were used in accordance with protocols approved by the Institutional Animal Care and Use Committee at the University of Arkansas for Medical Sciences. The experiments involved murine mesentery, which represents an ideal animal model for proof-of-concept of optical imaging of lymphatic vessels in vivo because it consists of very thin relatively transparent low-light-scattering tissue with a single layer of separate and clearly notable lymph microvessels. The preparation procedure is safe and does not affect cell properties for at least 5 h (ref. 37). After induction of standard anaesthesia with ketamine/xylazine, 50/10 mg kg^{-1}, i.m., the animal was laparotomized by a midabdominal incision, and the small-intestinal mesentery was placed on a customized, heated (37.7 °C) microscope stage and suffused with warmed Ringer's solution (37 °C, pH 7.4) containing 1% bovine serum albumin to prevent protein loss. A 10 ml solution of unconjugated GNTs (0.2 mg ml^{-1}) or GNTs with antibodies (0.2 mg ml^{-1}) in phosphate buffered saline, both containing equivalent concentration of nanoparticles, were topically applied on the area of murine mesentery with a lymph vessel.

Integrated PA/PT microscopy

Laser-induced PT and accompanying PA and bubble-formation phenomena in GNTs were evaluated using an integrated PA/PT microscope as described in detail elsewhere[12,16,36] (see Supplementary Methods and Supplementary Fig. S2). Briefly, this setup was built on the technical platform of an upright Olympus BX51 microscope (Olympus America). A tunable pulse laser parametric oscillator (Lotis) was used to irradiate samples either in microscopic slides with thick (120 mm) or thin (,1 mm) layer of GNT suspension or mouse mesentery and mouse skin with the following parameters: wavelength, 420–2,300 nm; pulse width, 8 ns; beam diameter, 2–50 μm; fluence range, 1 to 1×10^4 mJ cm^2; pulse repetition rate, 10–50 Hz.

Laser-induced PA waves (referred to as PA signals) were detected with an ultrasound transducer (XMS-310, 10 MHz, Panametrics) gently attached to the slide or to the mesentery structure through a thin layer of warm water. After amplification (amplifier model #5662, gain 60 dB, Panametrics), the PA signals were recorded with a Boxcar technique (Stanford Research Systems) and a Tektronix TDS 3032B oscilloscope, and then analysed with standard and customized software.

In thermolens mode, laser-induced temperature-dependent variations of the refractive index around GNTs in a liquid environment caused the defocusing of a collinear helium–neon laser probe beam (model #117A, Spectra-Physics; wavelength, 633 nm; 1.4 mW) and a subsequent reduction in the beam's intensity at its centre, detected with a photodiode (C5658; Hamamatsu Corp.). In PT imaging mode, the refractive index variations were visualized using a second, laser probe pulse (Raman Shifter; wavelength, 639 nm; pulse width, 12 ns; pulse energy, 2 nJ; 0–10 μs delay) and a charge coupled device (CCD) camera (Apogee)[12]. The target area was subjected to PA/PT scanning using an automatic microscopic stage (Conix Research) and visual basic software with a total scanning time of 6 min.

Statistical analysis

Results are expressed as means+the standard error (s.e.) of at least three independent experiments (P,0.05). Statistica 5.11 (StatSoft) and MATLAB 7.0.1 (MathWorks) were used for the statistical calculations. Data were summarized as the mean, standard deviation (s.d.), median, interquartile range and full range. Comparisons of PA and PT data were carried out using a scatterplot in conjunction with Spearman correlation analysis. Particle size analyses in the AFM images were carried out using the 'Particle Analysis' as well as 'Section' parameters in the Nanoscope Software. The numbers of particles used for analyses were 1×10^2 particles.

Supplementary Material

Refer to Web version on PubMed Central for supplementary material.

Acknowledgments

This work was supported in part by National Institute of Health grant nos R01EB000873, R01EB009230, R01CA131164, R21EB005123 and R21CA139373, National Science Foundation grant nos DBI-0852737 and CMMI-0709121 and the Arkansas Biosciences Institute. The authors thank R. Goforth and R. Deaton for their helpful discussions regarding this study. The authors also thank D. Lapotko for his assistance in setting up the PT microscope, N. Khlebtsov for providing gold nanorods and gold nanoshells, H.-J. Kim for her assistance in image processing and T.F. Garrison, J.-H. Kim, N. Kotagiri and J.S. Lee for their assistance with AFM and TEM imaging and sample preparation.

References

1. Zharov VP, Galitovsky V, Viegas M. Photothermal detection of local thermal effects during selective nanophotothermolysis. Appl. Phys. Lett. 2003; 83:4897–4899.
2. Hirsch LR, et al. Nanoshell-mediated near-infrared thermal therapy of tumors under magnetic resonance guidance. Proc. Natl Acad. Sci. USA. 2003; 100:13549–13554. [PubMed: 14597719]
3. Zharov VP, Galitovskaya EN, Jonson C, Kelly T. Synergistic enhancement of selective nanophotothermolysis with gold nanoclusters: potential for cancer therapy. Laser Surg. Med. 2005; 37:219–226.
4. Huang X, El-Sayed IH, Qian W, El-Sayed MA. Cancer cell imaging and photothermal therapy in the near-infrared region by using gold nanorods. J. Am. Chem. Soc. 2006; 128:2115–2120. [PubMed: 16464114]
5. Zharov VP, Mercer KE, Galitovskaya EN, Smeltzer MS. Photothermal nanotherapeutics and nanodiagnostics for selective killing of bacteria targeted with gold nanoparticles. Biophys. J. 2006; 90:619–627. [PubMed: 16239330]
6. Everts M, et al. Covalently linked Au nanoparticles to a viral vector: potential for combined photothermal and gene cancer therapy. Nano Lett. 2006; 6:587–591. [PubMed: 16608249]

7. Khlebtsov BN, Zharov VP, Melnikov AG, Tuchin VV, Khlebtsov NG. Optical amplification of photothermal therapy with gold nanoparticles and nanoclusters. Nanotechnology. 2006; 17:5167–5179.
8. Gobin AM, et al. Near-infrared resonant nanoshells for combined optical imaging and photothermal cancer therapy. Nano Lett. 2007; 7:1929–1934. [PubMed: 17550297]
9. Chen J, et al. Immuno gold nanocages with tailored optical properties for targeted photothermal destruction of cancer cells. Nano Lett. 2007; 7:1318–1322. [PubMed: 17430005]
10. Eghtedari M, et al. High sensitivity of in vivo detection of gold nanorods using a laser optoacoustic imaging system. Nano Lett. 2007; 7:1914–1918. [PubMed: 17570730]
11. Zharov VP, Kim J-W, Everts M, Curiel DT. Self-assembling nanoclusters in living systems: application for integrated photothermal nanodiagnostics and nanotherapy. Nanomedicine. 2005; 1:326–345. [PubMed: 17292107]
12. Zharov VP, Lapotko DO. Photothermal imaging of nanoparticles and cells. IEEE. J. Sel. Top. Quant. Electron. 2005; 11:733–751.
13. Pissuwan D, Valenzuela SM, Cortie MB. Therapeutic possibilities of plasmonically heated gold nanoparticles. Trends Biotechnol. 2006; 24:62–67. [PubMed: 16380179]
14. Xu M, Wang LV. Photoacoustic imaging in biomedicine. Rev. Sci. Instrum. 2006; 77 041101.
15. Huang X, Jain PK, El-Sayed IH, El-Sayed MA. Plasmonic photothermal therapy (PPTT) using gold nanoparticles. Laser Med. Sci. 2008; 23:217–228.
16. Zharov VP, Galanzha EI, Shashkov EV, Khlebtsov N, Tuchin V. In vivo photoacoustic flow cytometry for monitoring circulating single cancer cells and contrast agents. Opt. Lett. 2006; 31:3623–3625. [PubMed: 17130924]
17. Kam NWS, O'Connell M, Wisdom JA, Dai H. Carbon nanotubes as multifunctional biological transporters and near-infrared agents for selective cancer cell destruction. Proc. Natl Acad. Sci. USA. 2005; 102:11600–11605. [PubMed: 16087878]
18. Zharov VP, et al. Photoacoustic flow cytometry: principle and application for real-time detection of circulating single nanoparticles, pathogens and contrast dyes in vivo. J. Biomed. Opt. 2007; 12 051503.
19. Kim J-W, Galanzha EI, Shashkov EV, Kotagiri N, Zharov VP. Photothermal antimicrobial nanotherapy and nanodiagnostics with selfassembling carbon nanotube clusters. Laser Surg. Med. 2007; 39:622–634.
20. Galanzha EI, Shashkov EV, Tuchin VV, Zharov VP. In vivo multiparameter multispectral photoacoustic lymph flow cytometry with natural cell focusing, label-free detection and multicolor nanoparticle probes. Cytometry A. 2008; 73:884–894. [PubMed: 18677768]
21. Zerda A, et al. Carbon nanotubes as photoacoustic molecular imaging agents in living mice. Nature Nanotech. 2008; 3:557–562.
22. Poland CA, et al. Carbon nanotubes introduced into the abdominal cavity of mice show asbestos-like pathogenicity in a pilot study. Nature Nanotech. 2008; 3:423–428.
23. Schipper ML, et al. A pilot toxicology study of single-walled carbon nanotubes in a small sample of mice. Nature Nanotech. 2008; 3:216–221.
24. Alitalo K, Tammela T, Petrova TV. Lymphangiogenesis in development and human disease. Nature. 2005; 438:946–953. [PubMed: 16355212]
25. Karpanen T, Alitalo K. Molecular biology and pathology of lymphangiogenesis. Annu. Rev. Pathol. 2008; 3:367–397. [PubMed: 18039141]
26. Brown P. Lymphatic system: unlocking the drains. Nature. 2005; 436:456–458. [PubMed: 16049446]
27. Christofori G. New signals from the invasive front. Nature. 2006; 441:444–450. [PubMed: 16724056]
28. Cueni LN, Detmar M. New insights into the molecular control of the lymphatic vascular system and its role in disease. J. Invest. Dermatol. 2006; 126:2167–2177. [PubMed: 16983326]
29. Prevo R, Banerji S, Ferguson DJ, Clasper S, Jackson DG. Mouse LYVE-1 is an endocytic receptor for hyaluronan in lymphatic endothelium. J. Biol. Chem. 2001; 276:19420–19430. [PubMed: 11278811]

30. McElroy M, et al. Fluorescent LYVE-1 antibody to image dynamically lymphatic trafficking of cancer cells in vivo. J. Surg. Res. 2009; 151:68–73. [PubMed: 18599080]
31. Slavik, J. Fluorescence Microscopy and Fluorescent Probes. Plenum Press; 1996.
32. Contag PR, Olomu IN, Stevenson DK, Contag CH. Bioluminescent indicators in living mammals. Nature Med. 1998; 4:245–247. [PubMed: 9461201]
33. Nolte MA, Kraal G, Mebius RE. Effects of fluorescent and nonfluorescent tracing methods on lymphocyte migration in vivo. Cytometry A. 2004; 61:35–44. [PubMed: 15351987]
34. Zhang JL, Yokoyama S, Ohhashi T. Inhibitory effects of fluorescein isothiocyanate photoactivation on lymphatic pump activity. Microvasc. Res. 1997; 54:99–107. [PubMed: 9327381]
35. American National Standard for Safe Use of Lasers. ANSI. 2000; Z136:1.
36. Shashkov EV, Everts M, Galanzha EI, Zharov VP. Quantum dots as multimodal photoacoustic and photothermal contrast agents. Nano Lett. 2008; 8:3953–3958. [PubMed: 18834183]
37. Galanzha EI, Tuchin VV, Zharov VP. Advances in small animal mesentery models for in vivo flow cytometry, dynamic microscopy and drug screening (review). World J Gastroenterol. 2007; 13:192–218. [PubMed: 17226898]
38. Murphy CJ, et al. Gold nanoparticles in biology: beyond toxicity to cellular imaging. Acc. Chem. Res. 2008; 41:1721–1730. [PubMed: 18712884]
39. Lewinski N, Colvin V, Drezek R. Cytotoxicity of nanoparticles. Small. 2008; 4:26–49. [PubMed: 18165959]
40. Jan E, et al. High-content screening as a universal tool for fingerprinting of cytotoxicity of nanoparticles. ACS Nano. 2008; 2:928–938. [PubMed: 19206490]
41. Pernodet N, et al. Effects of citrate/gold nanoparticles on human dermal fibroblasts. Small. 2006; 2:766–773. [PubMed: 17193121]
42. Shukla R, et al. Biocompatibility of gold nanoparticles and their endocytotic fate inside the cellular compartment: a microscopic overview. Langmuir. 2005; 21:10644–10654. [PubMed: 16262332]
43. Connor EE, Mwamuka J, Gole A, Murphy CJ, Wyatt MD. Gold nanoparticles are taken up by human cells but do not cause acute cytotoxicity. Small. 2005; 1:325–327. [PubMed: 17193451]
44. Swanson JN. Repeated colloidal gold tests in rheumatoid arthritis. Ann. Rheum. Dis. 1949; 8:232–237. [PubMed: 18623821]
45. Smith BR, et al. Real-time intravital imaging of RGD-quantum dot binding to luminal endothelium in mouse tumor neovasculature. Nano Lett. 2008; 8:2599–2606. [PubMed: 18386933]
46. Valadon P, et al. Screening phage display libraries for organ-specific vascular immunotargeting in vivo. Proc. Natl Acad. Sci. USA. 2006; 103:407–412. [PubMed: 16384919]
47. He W, Wang H, Hartmann LC, Cheng JX, Low PS. In vivo quantitation of rare circulating tumor cells by multiphoton intravital flow cytometry. Proc. Natl Acad. Sci. USA. 2007; 104:11760–11765. [PubMed: 17601776]
48. Padera TP, et al. Lymphatic metastasis in the absence of functional intratumor lymphatics. Science. 2002; 296:1883–1886. [PubMed: 11976409]
49. Partanen TA, Paavonen K. Lymphatic versus blood vascular endothelial growth factors and receptors in humans. Microsc. Res. Tech. 2001; 55:108–121. [PubMed: 11596156]
50. Kim J-W, Kotagiri N, Kim J-H, Deaton R. In situ fluorescence microscopy visualization and characterization of nanometer-scale carbon nanotubes labeled with 1-pyrenebutanoic acid, succinimidyl ester. Appl. Phys. Lett. 2006; 88 213110.

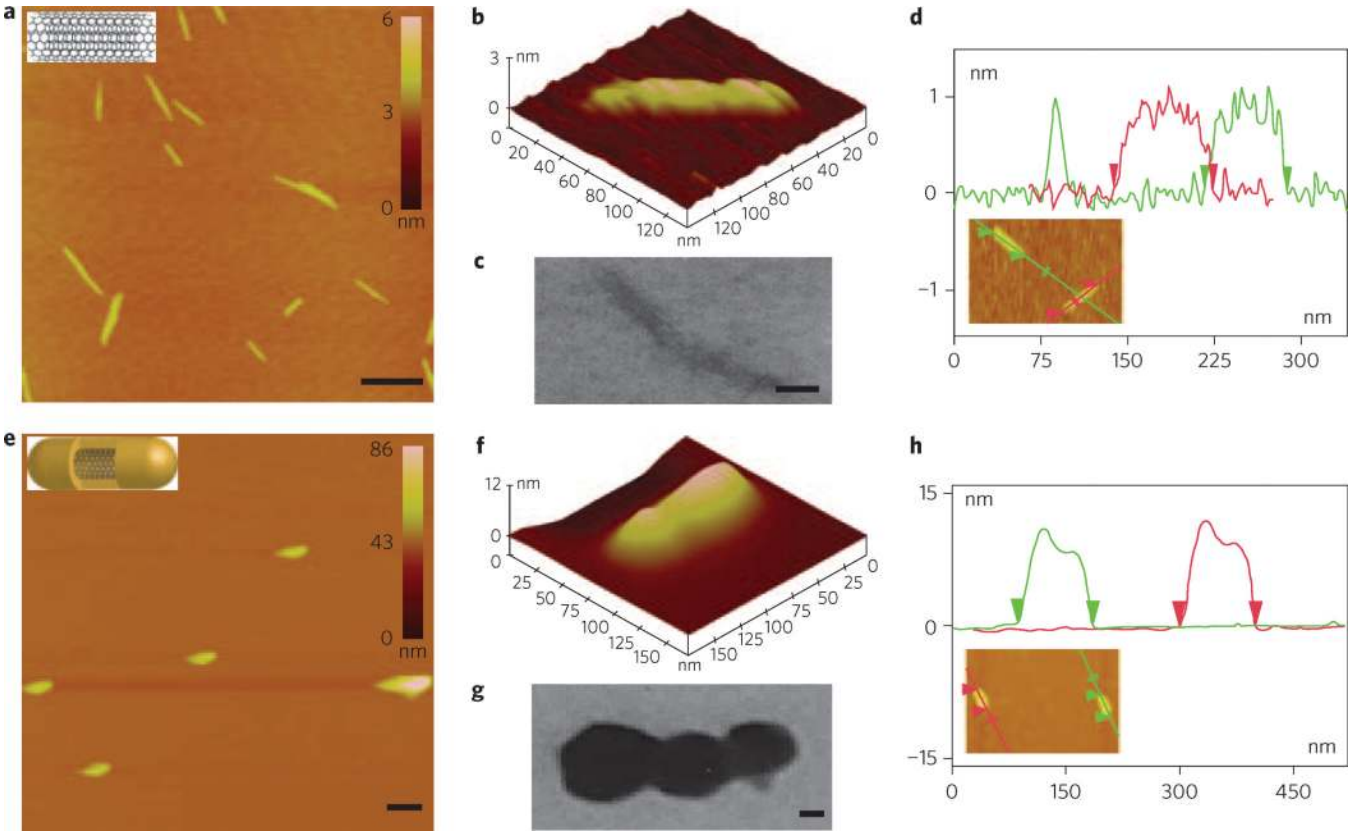

Figure 1. AFM and TEM image analyses

a–h, Results for single-walled carbon nanotubes (**a–d**) and GNTs (**e–h**). Topographic AFM images (**a,e**); surface plots (45° view) of magnified topographic images of **a** and **e** (**b,f**); TEM images (**c,g**); AFM section analysis results (**d,h**). Scale bars, 100 nm for AFM images (**a,e**) and 10 nm for TEM images (**c,g**).

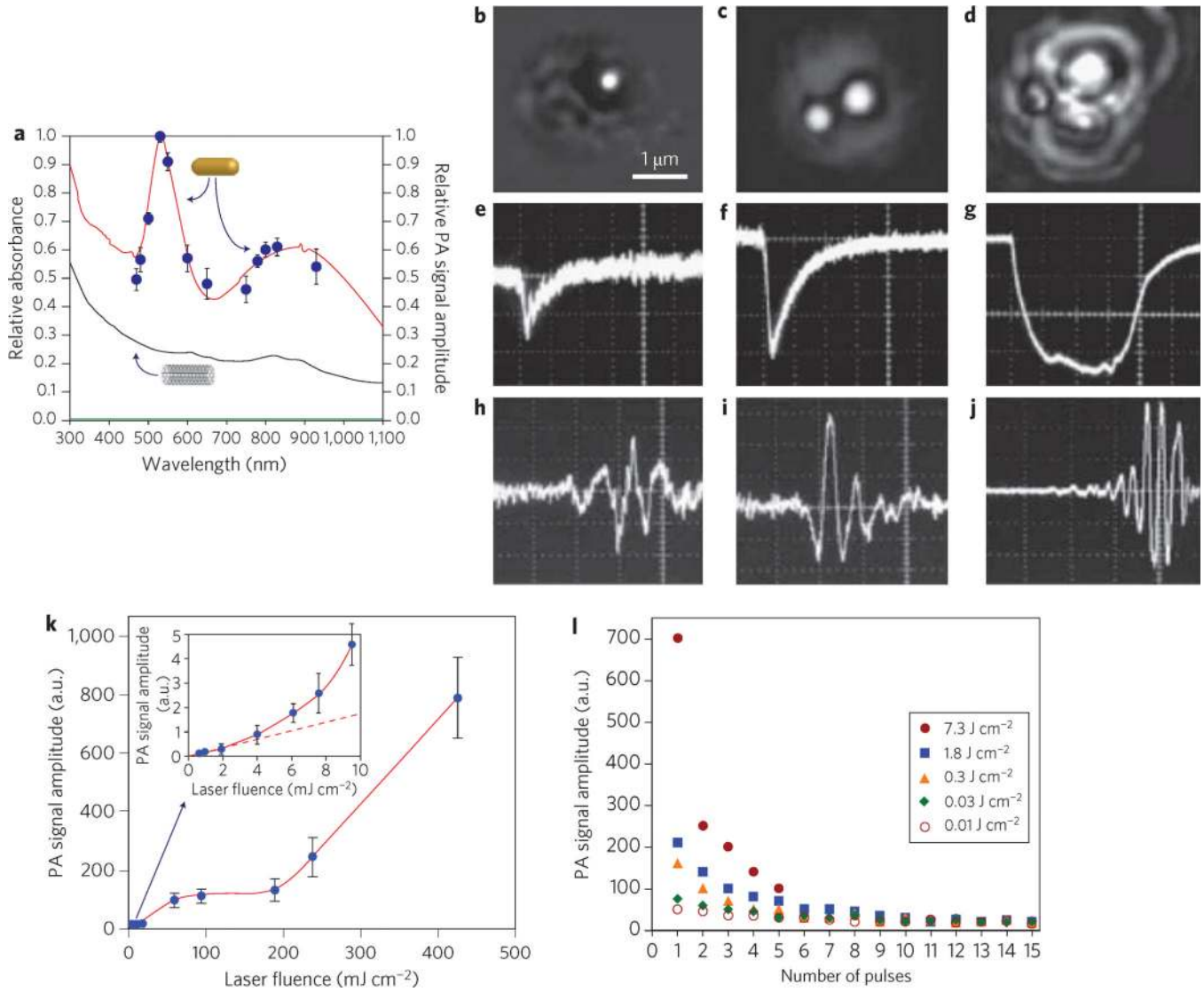

Figure 2. Absorption spectra of carbon nanotubes and GNTs, and PA and PT analyses of GNTs

a, Normalized optical spectra (left vertical axis) of GNTs in ddH_2O (red line), shortened single-walled carbon nanotubes in ddH_2O (black line) and ddH_2O only (green line) and normalized PA signal amplitudes (right vertical axis) of GNTs in ddH_2O (blue circles) at different laser wavelengths. The concentration of carbon nanotubes was ~35 times higher than that of GNTs. **b–j**, PT images (**b–d**), PT thermolens signals (**e–g**) and PA signals (**h–j**) from GNTs under a single laser pulse at 850 nm. The laser fluence and time delay were 10 mJ cm^{-2} and 5 ns (**b**), 55 mJ cm^{-2} and 5 ns (**c**) and 0.2 J cm^{-2} and 70 ns (**d**). Amplitude (vertical axis), timescale (horizontal axis) and laser fluence were 25 mV, 1 ms div^{-1} and 20 mJ cm^{-2} (**e**), 200 mV, 1 ms div^{-1} and 60 mJ cm^{-2} (**f**), 500 mV, 2 ms div^{-1} and 0.2 J cm^{-2} (**g**), 50 mV, 2 ms div^{-1} and 15 mJ cm^{-2} (**h**), 100 mV, 1 ms div^{-1} and 55 mJ cm^{-2} (**i**), and 500 mV, 2 ms div^{-1} and 0.2 J cm^{-2} (**j**). **k**, PA signal amplitudes from GNTs as a function of laser fluence. Inset: detailed linear and nonlinear signal behaviour at low laser fluences. **l**, PA signals from GNTs as function of laser pulse number at 850 nm and under various laser fluences. The error bars represent the standard deviation in five measurements.

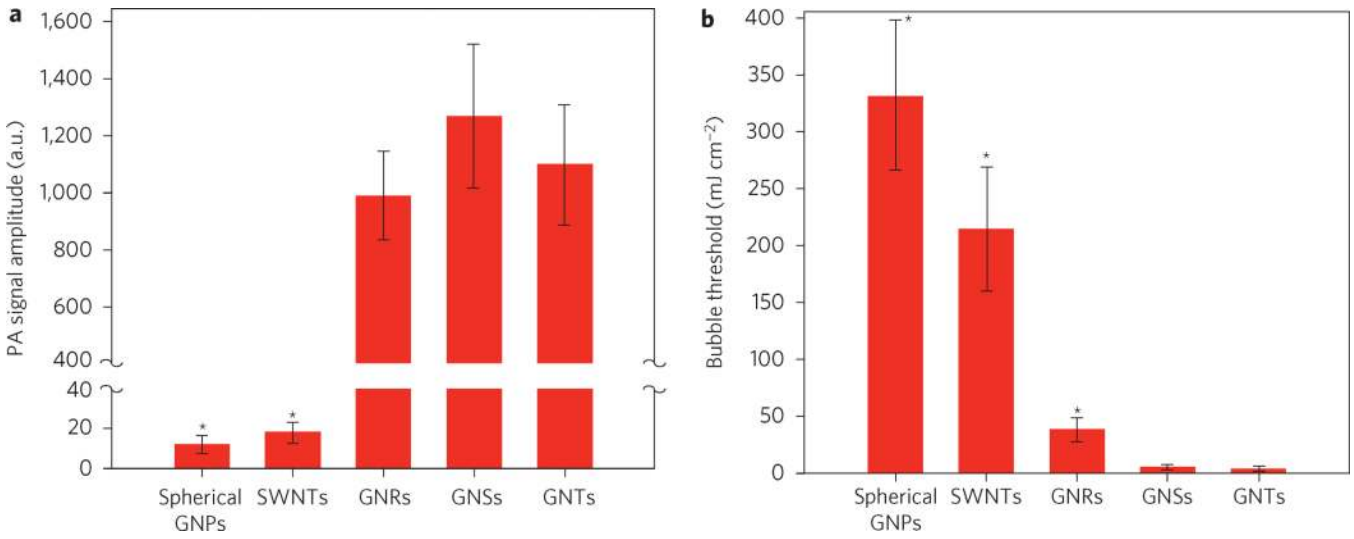

Figure 3. Comparison of PA signals and bubble thresholds among various nanoparticles

a,b, PA signal amplitudes (**a**) and bubble-formation thresholds (**b**) of spherical gold nanoparticles (GNPs, 40 nm in diameter), single-walled carbon nanotubes (SWNTs, 1.7 nm× 186 nm), gold nanorods (GNRs, 15 nm×52 nm), gold nanoshells (GNSs, 140-nm silica core with 8-nm gold shell), and GNTs (11 nm × 99 nm) in ddH_2O at a concentration of 1×10^{11} particles ml^{-1} and under a single laser pulse. Laser fluence was ~100 mJ cm^{-2} (a). Laser wavelengths were 532 nm for spherical GNPs and 850 nm for the remainder of the nanoparticles. The error bars represent the standard deviation in ten measurements. *P<0.05, compared to GNTs.

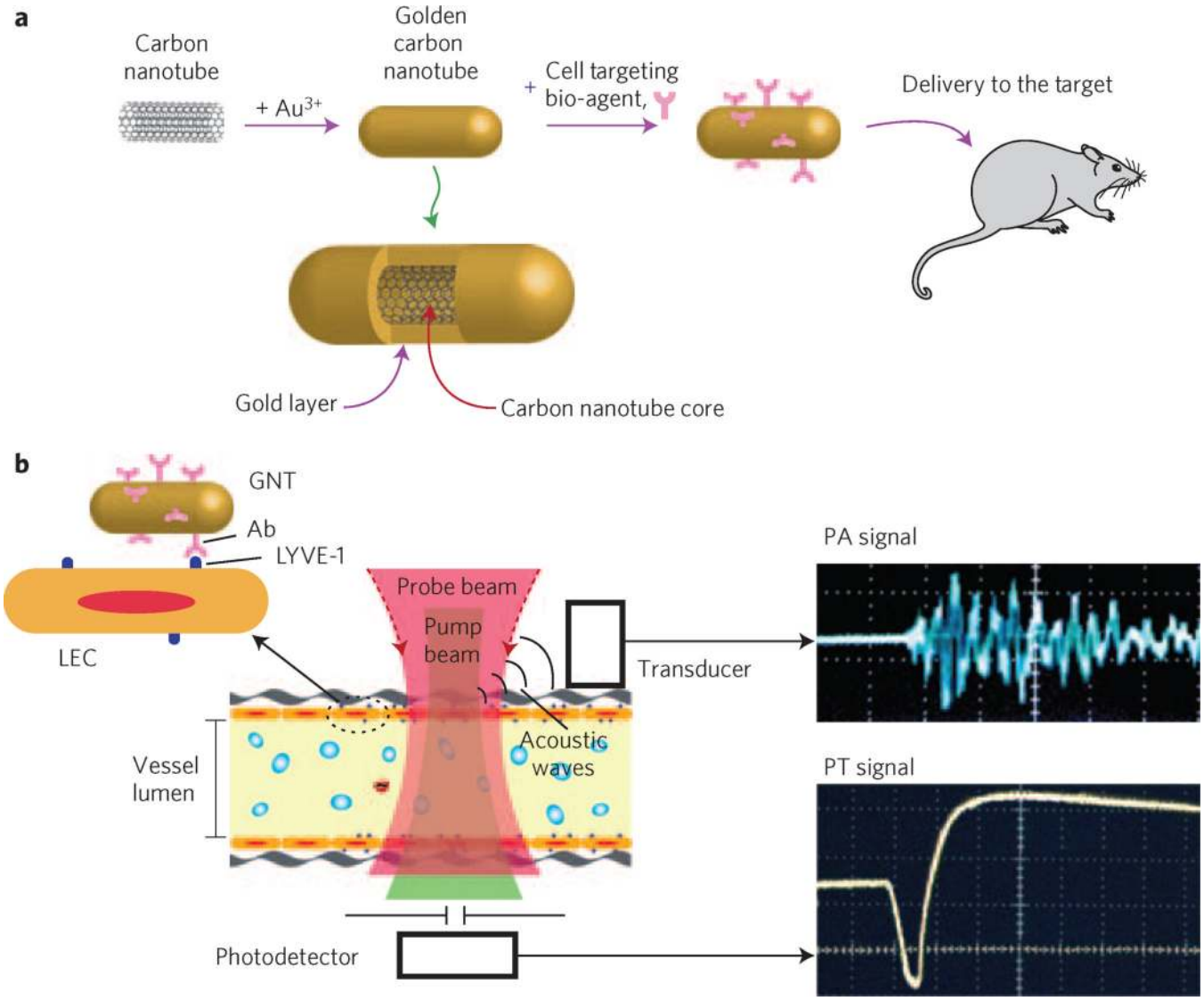

Figure 4. Schematics of GNT-assisted PA/PT molecular diagnostics and therapeutics

a, GNT synthesis and its delivery to the target. **b**, Principle of targeting endothelial LYVE-1 receptors with antibody–GNT complex (left panel), and PA (top right) and PT (bottom right) detection schematics.

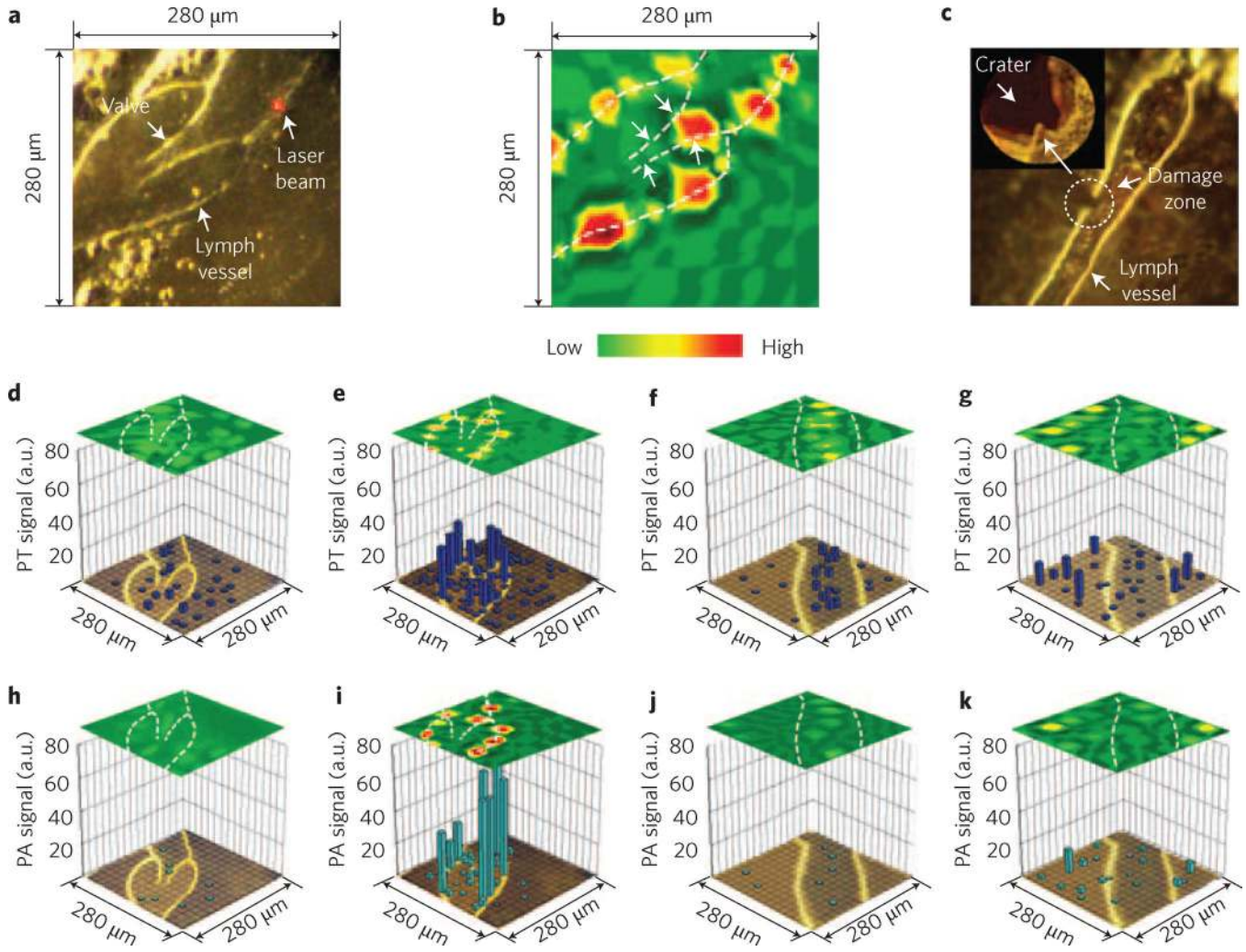

Figure 5. In vivo molecular targeting of murine lymphatics with GNTs guided by an integrated PA/PT technique

a, Fragment of mouse mesentery with mapping area (square, 280 mm_ 280 mm). **b**, Enlarged version of **i. c**, Laser-induced localized (~10 μm in diameter) lymphatic wall damage. **d–k,** PT (**d–g**) and PA (**h–k**) two-dimensional lymphatic mapping in selected mesenteric area before GNT administration (**d,h**), at 60 min after administration of antibody–GNTs (**e,i**) and at 15 min (**f,j**) and 60min (**g,k**) after administration of GNTs alone. Dashed white lines in **d–k** indicate the lymphatic wall and valve. Arrows in **b** indicate valve leaflets. Total scanning time was 16 s. Laser parameters: wavelength, 850 nm; fluences, 35 mJ cm^{-2} (**d,h**), 10 mJ cm^{-2} (**e–g, i–k**) and 60 mJ cm^{-2} (**c**).